Journal of Materials Chemistry A

PAPER

View Article Online
View Journal | View Issue

Cite this: J. Mater. Chem. A, 2016, 4, 2461

$YCuTe_2$: a member of a new class of thermoelectric materials with $CuTe_4$-based layered structure†

Umut Aydemir,*[ab] Jan-Hendrik Pöhls,[c] Hong Zhu,[de] Geoffroy Hautier,[f] Saurabh Bajaj,[a] Zachary M. Gibbs,[a] Wei Chen,[gh] Guodong Li,[ab] Saneyuki Ohno,[ab] Danny Broberg,[i] Stephen Dongmin Kang,[ab] Mark Asta,[i] Gerbrand Ceder,[dgi] Mary Anne White,[c] Kristin Persson,[gi] Anubhav Jain[g] and G. Jeffrey Snyder*[ab]

Received 16th December 2015
Accepted 22nd January 2016

DOI: 10.1039/c5ta10330d

www.rsc.org/MaterialsA

Intrinsically doped samples of $YCuTe_2$ were prepared by solid state reaction of the elements. Based on the differential scanning calorimetry and the high temperature X-ray diffraction analyses, $YCuTe_2$ exhibits a first order phase transition at ~440 K from a low-temperature-phase crystallizing in the space group $P\bar{3}m1$ to a high-temperature-phase in $P\bar{3}$. Above the phase transition temperature, partially ordered Cu atoms become completely disordered in the crystal structure. Small increases to the Cu content are observed to favour the formation of the high temperature phase. We find no indication of superionic Cu ions as for binary copper chalcogenides (*e.g.*, Cu_2Se or Cu_2Te). All investigated samples exhibit very low thermal conductivities (as low as ~0.5 W m^{-1} K^{-1} at 800 K) due to highly disordered Cu atoms. Electronic structure calculations are employed to better understand the high thermoelectric efficiency for $YCuTe_2$. The maximum thermoelectric figure of merit, zT, is measured to be ~0.75 at 780 K for $Y_{0.96}Cu_{1.08}Te_2$, which is promising for mid-temperature thermoelectric applications.

1. Introduction

A sustainable solution for the energy crisis requires both replacing fossil fuels and diversifying our energy resources. As more than half the energy produced by home heating, automotive exhaust, and industrial processes is lost as waste heat, the recovery of even a very small amount of this energy would greatly contribute to global energy solutions.[1] In this sense, thermoelectric materials, which convert waste heat into useful electrical energy, possess great potential as a sustainable and reliable energy source. Thermoelectric waste heat recovery is a proven technology and has been successfully implemented in deep space exploration missions for decades. However, to broaden the application areas, lower cost and improved thermoelectric efficiencies are required.

The thermoelectric efficiency of a material depends on the dimensionless thermoelectric figure of merit, $zT = S^2T/\kappa\rho$, where T is the absolute temperature, S is Seebeck coefficient (thermopower), ρ is electrical resistivity, and κ is the total thermal conductivity.[2] The latter is comprised of three components: the electronic contribution, κ_e (related to ρ for metals through the Wiedemann–Franz law, $\kappa_e = LT/\rho$, where L is the Lorenz number), due to either electrons or holes; the bipolar contribution, κ_B, due to both electrons and holes; and the lattice contribution, κ_L, due to quantized lattice vibrations (phonons). κ_L should be low or lowered to achieve high thermoelectric efficiency. Reductions in κ_L can be achieved by shortening the mean free path of the lattice phonons with several strategies such as point defect scattering, alloy scattering, grain-boundary scattering or interface scattering.[3] However, some materials, such as clathrates,[4,5] skutterudites,[6] and zintl pnictides[7,8] display intrinsically low lattice thermal conductivities associated with their structures and lattice dynamics. Apart from κ_L which can, to some extent, be manipulated independently, all other parameters in the thermoelectric efficiency equation are interdependent and governed by the charge carrier concentration, n. The optimum carrier concentrations for high

[a]Department of Applied Physics and Materials Science, California Institute of Technology, 1200 E California Blvd, Pasadena, CA, USA
[b]Department of Materials Science and Engineering, Northwestern University, 2220 Campus Drive, Evanston, IL, USA. E-mail: umut.aydemir@northwestern.edu; jeff.snyder@northwestern.edu
[c]Department of Physics and Atmospheric Science, Dalhousie University, 6310 Coburg Rd, PO BOX 15000, Halifax, NS, B3H 4R2 Canada
[d]Department of Materials Science and Engineering, Massachusetts Institute of Technology, 77 Massachusetts Avenue, Massachusetts, MA, USA
[e]University of Michigan – Shanghai Jiao Tong University Joint Institute, Shanghai Jiao Tong University, Shanghai 200240, China
[f]Institute of Condensed Matter and Nanosciences (IMCN), Université catholique de Louvain, Chemin des étoiles 8, bte L7.03.01, Louvain-la-Neuve, Belgium
[g]Lawrence Berkeley National Lab, 1 Cyclotron Rd., Berkeley, CA, USA
[h]Department of Mechanical, Materials and Aerospace Engineering, Illinois Institute of Technology, Chicago, IL 60616, USA
[i]Department of Materials Science and Engineering, University of California Berkeley, Berkeley, CA, USA

† Electronic supplementary information (ESI) available: Details of EDS, crystal structure, band structure, experimental and theoretical calculation of transport data. See DOI: 10.1039/c5ta10330d

efficiencies are generally observed for heavily doped semiconductors ($n = 10^{19}$ to 10^{21} carriers cm^{-3}).[9]

We recently initiated a high-throughput search for new thermoelectric materials with high power factors, S^2/ρ, within the Materials Project (www.materialsproject.org) electronic structure database.[10] The bulk thermal conductivity was largely neglected in this first-order screening due to the computational costs associated with direct evaluation of this metric; however, minimum thermal conductivity estimates[11] were computed for many promising candidates. By assuming constant relaxation time for electron scattering, we revealed a new group of thermoelectric materials, XYZ_2 (X, Y: rare earth or transition metals, Z: group VI elements).[12] Among them, we previously reported the thermoelectric properties of $TmAgTe_2$ displaying extremely low thermal conductivity (0.2–0.3 W m^{-1} K^{-1} for $T > 600$ K, comparable to the glassy limit) but with high electrical resistivity due to low carrier concentrations ($\sim 10^{17}$ cm^{-3} at room temperature).[12] A higher carrier concentration was observed by Lin *et al.* for $TmCuTe_2$ crystallizing in a different crystal structure ($DyCuTe_2$ structure type)[13,14] from $TmAgTe_2$, leading to relatively high zT of 0.81 at 745 K.[15] The substitution of Ag with Cu might lead to an increase in carrier concentration due to intrinsic defects generally found for copper chalcogenides ($Cu_{2-x}Y$ (Y = S, Se, Te)).[16–21] Apart from copper vacancies, copper chalcogenides have attracted renewed attention mainly due to superionic Cu atoms with liquid-like mobility leading to extremely low thermal conductivity.[16–18,20] However, it was not reported whether this mechanism is responsible for the low thermal conductivity observed for the high temperature phase of $TmCuTe_2$. Inspired by our high-throughput calculations and reported results on $TmCuTe_2$, we synthesized $YCuTe_2$ (using the much cheaper and more abundant element Y) and characterized its thermoelectric properties. In this paper, we present the crystal structure, thermal behaviour, optical absorption, first-principles calculations, and electronic and thermal transport results of intrinsically doped $YCuTe_2$. Furthermore, we measured the heat capacity to investigate the potential superionic character of the Cu atoms in this material.

2. Experimental methods

2.1 Sample preparation

All synthetic procedures of $YCuTe_2$ were performed in an Ar-filled glove box. For preparation, stoichiometric amounts of Y pieces (Alfa Aesar, 99.9%), Cu slug (Alfa Aesar, 99.995%, oxygen free) and Te pieces (Alfa Aesar, 99.9999%) were vacuum sealed ($\sim 10^{-6}$ mbar) in carbon-coated fused silica ampoules and heated to 475 °C for 10 h, then heated to 800 °C for 15 h, to 1170 °C for 15 h, then annealed at 1170 °C for 15 h, cooled to 800 °C for 15 h, to 400 °C for 15 h, and finally cooled to 100 °C in 15 h; the furnace was turned off at this temperature. The resulting ingots were hand-ground in a glove box and placed in 1/2 inch diameter high-density graphite dies (POCO) for consolidation. The samples were hot-pressed at 600 °C for 1 h under 80 MPa pressure in Ar atmosphere. The pressed samples were cooled to room temperature over 2 h.

2.2 Sample characterization

Sample purities were monitored by X-ray diffraction (XRD) using a PANalytical X'Pert Pro diffractometer (45 kV, 40 mA, Cu-Kα radiation) with reflection mode. High-temperature XRD (HT-XRD) measurements were carried out under He atmosphere with a sealed high-temperature stage equipped in the same instrument.[22] The lattice parameters determinations and Rietveld refinements were performed using the WinCSD program.[23] The density of the samples was measured with Archimedes' principle. To investigate the microstructure and chemical composition (by energy dispersive X-ray spectroscopy, EDS) of the secondary phases, a scanning electron microscope (Zeiss 1550 VP Field Emission SEM equipped with Oxford X-Max SDD EDS system) was used. The chemical composition of the target phases was determined by microprobe analysis using wavelength dispersive X-ray spectroscopy (WDS, JEOL JXA – 8200 system). A TA Instruments™ Q200 differential scanning calorimeter (DSC) was used to determine potential phase transitions. DSC thermograms of samples ($m \sim 10$ to 30 mg, known to ± 0.02 mg), hermetically sealed in aluminium pans, were recorded with a constant scanning rate of 1 K min^{-1} (for transition temperatures of events) to 20 K min^{-1} (for ΔH determination), under N_2 atmosphere. The heat capacity was measured *via* the enthalpic method using the same DSC.[24] For the heat capacity studies (m $\sim$ 12 mg, known to ± 0.02 mg), 10 K intervals were recorded from 320 K to 530 K with a scanning rate of 2 K min^{-1}. Before and after each temperature step the calorimeter was held isothermally for 5 min. Three experiments were carried out to calculate the heat capacity. In the first run, an empty hermitically sealed aluminium pan was recorded to determine the background of the DSC and aluminium pans. In the next two runs, Al_2O_3 powder as a standard sample and $YCuTe_2$ were measured. For each temperature interval the background was subtracted from the standard sample and $YCuTe_2$, respectively, and the area, $F(\Delta H, t)$, was integrated over time. The heat capacity of $YCuTe_2$, $C_{p,YCuTe_2}$, was calculated by:

$$C_{p,YCuTe_2} = \frac{F(\Delta H, t)_{YCuTe_2}}{F(\Delta H, t)_{Al_2O_3}} \frac{m_{Al_2O_3}}{m_{YCuTe_2}} C_{p,Al_2O_3} \quad (1)$$

The heat capacity of the standard sample, C_{p,Al_2O_3}, was acquired from ref. 25. The heat capacity was calibrated with relaxation calorimetry using a Physical Property Measurement System (PPMS, from Quantum Design) in the temperature range from 270 K to 390 K under high vacuum ($<10^{-4}$ Torr). The relaxation technique is described in ref. 26. Thermogravimetric analysis (TGA) was conducted under constant Ar flow on a Netzsch STA 449 C Jupiter thermal analyser with a heating rate of 10 K min^{-1}.

The electronic band gaps of the target phases were determined from room temperature to 573 K using diffuse reflectance infrared Fourier transform spectroscopy (DRIFTS) obtained with a Nicolet 6700 FTIR spectrophotometer (Thermo Scientific) equipped with a Praying Mantis Diffuse Reflection accessory (Harrick) as described in a previous work.[27] The measured reflectance, R, was related by Kubelka-Munk theory to a value proportional to the absorption coefficient using: $F(R) = (1 - R)^2/2R$.

2.3 Measurements of transport properties

Electrical and thermal transport properties were measured from 300 to 800 K. The electrical resistivity and Hall coefficient measurements were performed using the van der Pauw technique under a magnetic field of 2 T using pressure-assisted tungsten electrodes.[28] The Seebeck coefficients of the materials were determined using chromel–Nb thermocouples by applying an oscillated temperature gradient of ±7.5 K.[29] Thermal diffusivity, D, measurements were performed with a Netzsch LFA 457 laser flash apparatus. Thermal conductivity was calculated using the relation: $\kappa = D \times d \times C_p$, where d is the density of material being investigated and C_p is the heat capacity determined here at constant pressure.[30] The longitudinal and transverse sound velocities were determined by ultrasonic measurements (Panametrics NDT 5800 pulser/receiver with a Tektronix TDS 1012 digital oscilloscope) at room temperature. Honey was used as a coupling agent.

2.4 Electronic structure calculations

Density functional theory (DFT) calculations in this work were performed using the Vienna Ab initio Simulation Package (VASP)[31] with the Perdew–Burke–Ernzerhof (PBE)[32] generalized gradient approximation (GGA)[33] and the projector augmented-wave (PAW)[34] method to model core states. The PAW potentials consider as valence the following electrons: $4s^2 4p^6 5s^2 4d^1$ for Y, $3p^6 3d^{10} 4s^1$ for Cu, and $5s^2 5p^4$ for Te. The cut-off energy of the plane wave basis was set to 520 eV, electron occupations were smeared using a Gaussian smearing width of 0.05 eV, and integrations over the first Brillouin zone were made using k-point grid sets of $9 \times 11 \times 8$ and $5 \times 10 \times 6$ for the $P\bar{3}m1$ and $P\bar{3}$ phases, respectively, generated according to the Monkhorst–Pack scheme.[35] The elastic tensor and moduli were calculated following the stress–strain method.[36]

The electronic transport calculations were performed using the Boltztrap code[37] under a constant relaxation time approximation of 10^{-14} s. The Grüneisen parameter (γ) was calculated using the Vaschenko–Zubarev formulation ($\gamma = K'/2 - 5/6$, in which K' *is* the pressure derivative of the bulk modulus, K)[38] and fitting the total energy of the relaxed structure at different volumes to the Murnaghan equation of state, $(E(V) = E(V_0) + \frac{KV}{K'}\left[\frac{(V_0/V)^{K'}}{K'-1} + 1\right] - \frac{KV_0}{K'-1}$, in which V_0 is the equilibrium volume).[39] To compute the average effective mass tensor, we followed the method we developed before,[40] which is based on the Boltztrap results and implemented in pymatgen. This approach takes into account nonparabolicity, anisotropy, and the competitions of pockets in the Brillouin zone. Workflows were executed using the pymatgen[41] and FireWorks[42] software libraries.

3. Results and discussion

3.1 Phase analysis

Intrinsically doped $YCuTe_2$ samples were synthesized by solid state reaction of the elements and the resulting target materials were obtained either almost as single phase or together with Y_2Te (EDS composition) and YCu_xTe_{3-x} (ref. 43) as by-products (Fig. 1). The chemical compositions of the target phases are presented in Table 1. Compared with the nominal compositions, the WDS results indicate that as the nominal copper content increases, the Y content of the samples decreases leading to Y-deficient compositions for compounds with Cu = 1.08. A complete phase diagram analysis could not be performed in this study as the observed phase Y_2Te has not been reported in the literature, and is the subject of an ongoing investigation. The EDS mapping of the elements for the $YCuTe_2$ sample indicates homogenously distributed Y, Cu, and Te atoms throughout the target phase region (see Fig. S1†). Based on the SEM investigation, Cu precipitation was not observed on the surfaces of the samples after the hot press and transport measurements, which was generally reported for super ionic Cu chalcogenides.[44]

Based on the TGA measurement, $YCuTe_2$ shows negligible mass loss (<0.1%) in the temperature range from 300 K to 550 K (Fig. 2a). The DSC thermogram indicates a broad phase transition from a low-temperature phase to a high-temperature phase with a peak temperature of ~440 K on heating (Fig. 2b; the onset temperature, which would be a more accurate transition temperature, is less clearly defined here due to the wide transition region). The transition is rather subtle: $\Delta H = 4.1 \pm 0.4\ \mathrm{J\ g^{-1}}$. The breadth of the anomaly in $YCuTe_2$ indicates either an intrinsic double transition with the second (minor) phase transition at slightly lower temperature, or transition from a single-phase region to a mixed-phase with change in phase fractions over a temperature range indicating discontinuous

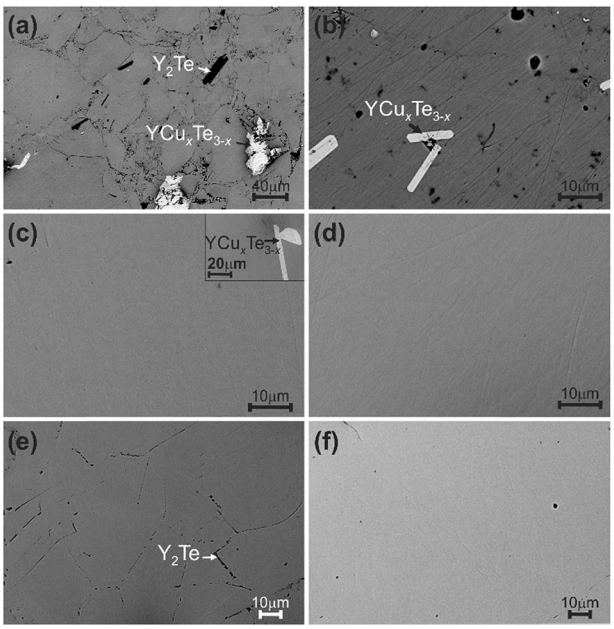

Fig. 1 SEM images of intrinsically doped $YCuTe_2$ samples: (a) $YCu_{0.96}Te_2$, (b) $Y_{0.98}CuTe_2$, (c) $YCuTe_2$, (d) $YCu_{1.04}Te_2$, (e) $YCu_{1.08}Te_2$, (f) $Y_{0.96}Cu_{1.08}Te_2$ in the backscattered electron imaging mode. The secondary phases of Y_2Te (EDS composition) and YTe_xCu_{3-x} precipitate at the grain boundaries and/or within the large grains of the target phases. With increasing Cu content there is a decrease in the secondary phase(s).

Table 1 The nominal and WDS compositions of the target phases together with standard uncertainties

Nominal compositions	WDS compositions
$YCu_{0.96}Te_2$	$Y_{1.075(4)}Cu_{0.948(5)}Te_{1.974(6)}$
$Y_{0.98}CuTe_2$	$Y_{1.080(4)}Cu_{0.957(5)}Te_{1.962(6)}$
$YCuTe_2$	$Y_{1.052(4)}Cu_{0.971(5)}Te_{1.977(6)}$
$YCu_{1.04}Te_2$	$Y_{1.043(4)}Cu_{0.983(5)}Te_{1.973(6)}$
$YCu_{1.08}Te_2$	$Y_{0.971(4)}Cu_{1.031(5)}Te_{1.998(6)}$
$Y_{0.96}Cu_{1.08}Te_2$	$Y_{0.973(4)}Cu_{1.0121(5)}Te_{2.015(6)}$

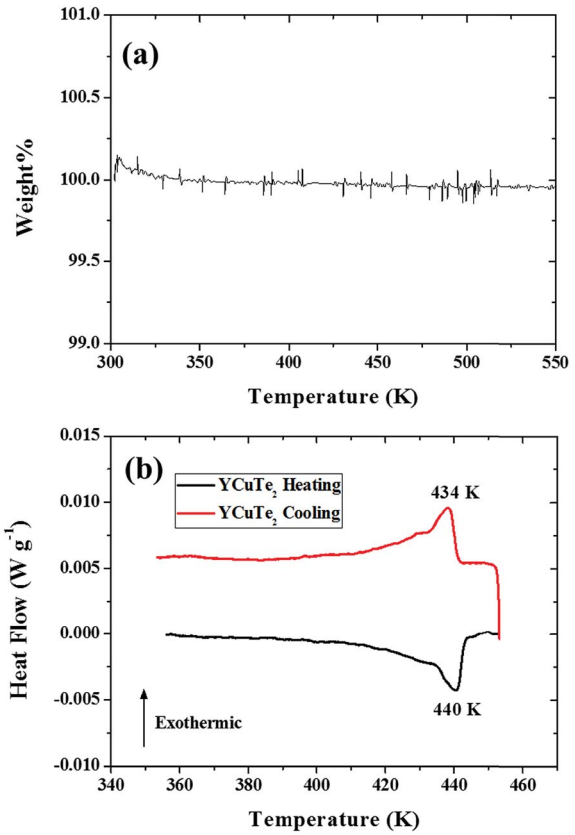

Fig. 2 (a) Thermogravimetric analysis of $YCuTe_2$ showing an insignificant mass loss (<0.1%) from room temperature to 550 K. (b) DSC thermogram of $YCuTe_2$ (scanning rate 1 K min^{-1}; mass 12.22 mg). $YCuTe_2$ shows a reversible, broad phase transition.

phase transition.[21] A broad exothermic peak also appears in the cooling cycle, indicating that the phase transition(s) is/are reversible. No additional phase transitions were recorded for $YCuTe_2$ in the temperature range from 300 K to 775 K. DSC of $Y_{0.96}Cu_{1.08}Te_2$ shows only a very minor anomaly at $T \sim 370$ K, confirmed by C_p measurements (see Section 3.4). $TmCuTe_2$ also shows a first order phase transition at ~600 K.[15] Copper chalcogenides, in comparison, undergo several phase transitions: Cu_2S at ~370 and ~700 K,[16] Cu_2Se at ~414 K,[17,18,21] and Cu_2Te at five successive temperatures between 300 K and 900 K.[18,19]

3.2 Crystal structure

$YCuTe_2$ definitively displays two phases, a low-temperature-phase (LT-phase) and a high-temperature-phase (HT-phase). The crystal structures of the LT- and HT-phases were determined using powder X-ray diffraction (PXRD) data (Fig. 3). The detailed results of the Rietveld refinements are given in Tables S1–S4.† The crystal structure of the LT modification is isotypic to $DyCuTe_2$ structure type (space group $P\bar{3}m1$, Fig. 4a).[13] In this crystal structure, there are two Y ($2c$, $6i$), three Cu ($2d$, $2 \times 6i$) and four Te ($2 \times 2d$, $2 \times 6i$) Wyckoff sites. All Y and Te positions are fully occupied along with the Cu $2d$ position, whereas the two $6i$ sites out of three Cu positions are partially occupied (see Table S1†). The crystal structure of LT-$YCuTe_2$ can be described as honeycomb-like channels formed by Cu and Te atoms along the c-axis in which Y atoms are aligned. This crystal structure can be alternatively considered as a $2a \times 2a \times 2c$ supercell of the $CaAl_2Si_2$ structure type.[45] By analogy to $CaAl_2Si_2$, Y and Cu atoms are all octahedrally (NiAs-like) and tetrahedrally (wurtzite-like) coordinated by Te atoms, respectively (see Table S3†). There are two types of $CuTe_4$ based layers that are stacked along the c-axis with A–B–A sequence. Layer-A is formed by ordered Cu1 atoms at the $2d$ site and disordered Cu3 atoms at the $6i$ site, while layer-B comprises disordered Cu2 atoms at the $6i$ site and vacant Cu positions. Unoccupied Cu positions destroy the chair-like six-membered rings, which would otherwise lead to two-dimensional infinite nets.

To understand the disorder of Cu atoms, we have performed DFT calculations on six configurations each for the LT- and HT-phase of $YCuTe_2$. These configurations were created using a $2 \times 1 \times 1$ supercell for each structure. Afterwards they were ranked according to electrostatic energy as determined by the Ewald sum using the pymatgen library.[46] In the most stable configuration (see Fig. S2a†), the Cu and Te atoms form ladder-like

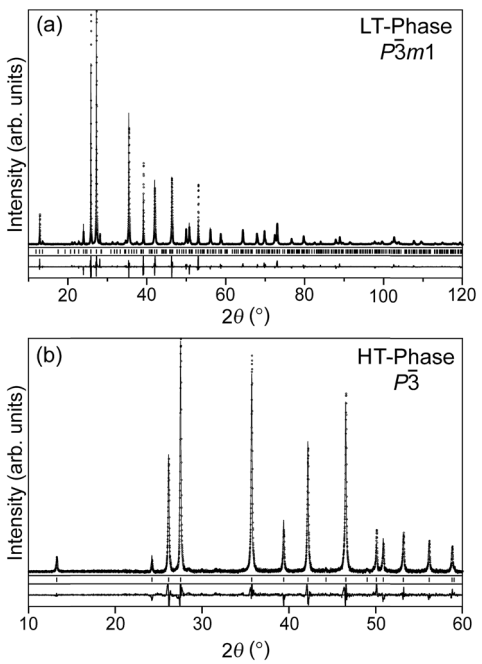

Fig. 3 Rietveld refinement plots for (a) LT-$YCu_{1.04}Te_2$ (room temperature) and (b) HT-$YCu_{1.04}Te_2$ (T = 493 K). Ticks mark the calculated reflection positions of the target phases and the baselines correspond to the residuals of the Rietveld refinements.

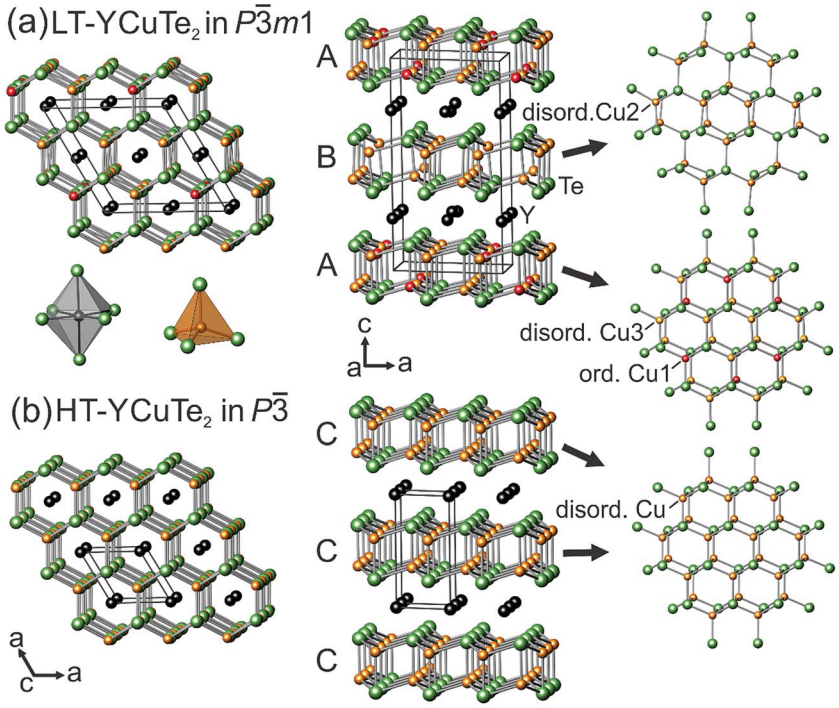

Fig. 4 Crystal structures of the (a) low-temperature (LT) and (b) high-temperature (HT) structures of $YCuTe_2$ (Y atoms are shown in black, Cu atoms in red or orange, and Te atoms in green). The LT-phase exhibits a layered structure with an A–B–A stacking sequence formed by Cu and Te atoms. Y atoms are octahedrally coordinated and Cu atoms are tetrahedrally coordinated. In the LT-phase, Cu is partially ordered in the A-layer, whereas in the HT-phase Cu is completely disordered (C-layers). The crystallographic sites for the ordered Cu atoms are completely occupied, whereas they are partially occupied for the disordered ones.

moieties in which the Cu atoms are found farther apart (d_{Cu-Cu} = 3.34 Å) in the four membered nets. On the other hand, in the highest-energy configuration (see Fig. S2b†), the Cu atoms are placed closer to each other (d_{Cu-Cu} = 3.17 Å) and arranged with Te atoms to form channels accommodating Y atoms along the *c*-direction. The energy difference between the lowest and highest energy configurations for the $P\bar{3}m1$ phase is ~10 meV per atom. Additionally, the total energy of the LT-phase is lower than that of the HT-phase by ~0.7 meV per atom for all the calculated models, which is within the numerical tolerance of our calculations.

As discussed above, the LT-phase transforms to the HT-phase at ~440 K according to DSC results. The HT-phase crystallizes in the trigonal space group $P\bar{3}$ with a, b = 4.2970(2) Å and c = 6.9087(5) Å.[35] In this crystal structure, there is one Y (1*a*), one Cu (2*d*) and one Te (2*d*) Wyckoff site (see Tables S2 and S4†). During the Rietveld refinement, Y and Te sites were observed to be fully occupied, whereas the Cu site was partially occupied. Partially disordered Cu atoms in the LT-phase are completely disordered at the 2*d* site in the HT-phase (Fig. 4). The phase transformation was investigated by HT-XRD experiments using the $YCu_{1.04}Te_2$ sample (Fig. 5). Supercell reflections with very low intensity disappear at 453 K suggesting completely disordered Cu atoms at the HT-phase. Our results also indicate that small increases in the copper content might lead to stabilization of the HT-phase (Fig. 6), as the supercell reflections lose intensity with higher Cu content. This seems reasonable considering the very small energy difference between LT- and the HT-phases observed in the total energy calculations.

Landau's criteria were applied to reveal the nature of the phase transition,[47] and the transition was found to be of first order similar to $TmCuTe_2$.[15] In terms of concentration wave vectors,[48] the collection of ordering vectors include {0, 0, 1/2},

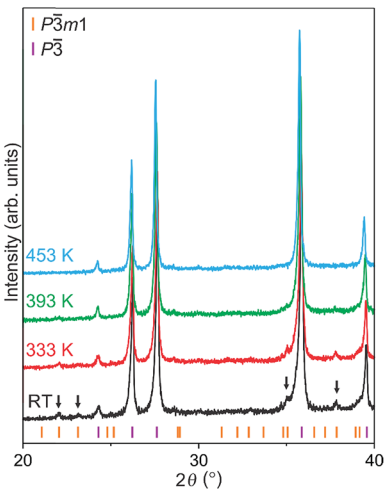

Fig. 5 HT-XRD patterns of $YCu_{1.04}Te_2$ sample. The intensity of the main supercell reflections indicated by arrows decreases with increasing temperature and vanishes completely at 453 K, *i.e.* above the phase transformation.

{1/2, 0, 0}, and {1/2, 0, 1/2} according to our structure model. These three add up to a reciprocal lattice vector, a condition which indicates a discontinuous phase transition.[48]

The lattice parameters were refined for the samples with varied Cu content and temperature (Fig. 7). For the former, the lattice parameters remain almost constant up to slightly above 25 at.% Cu and start to increase thereafter. For lower Cu content (YCu_xTe_2, $x < 1.04$), it is highly probable that the samples crystallize almost in the same chemical composition displaying very similar secondary phases, lattice parameters and transport properties (see Fig. 1, Table 1, and Sections 3.3 and 3.4). For higher Cu content ($x \geq 1.04$), additional Cu atoms may fill the vacant positions and expand the Cu–Te layers. Above room temperature (Fig. 7b), the unit cell length increases almost linearly in the *c*-direction while the unit cell length in the *a*-direction increases non-monotonically. The value of $c/a = 1.605$ is slightly smaller than ideal value for an hcp crystal structure (1.633) and remains constant until ~350 K, decreasing slightly close to the phase transition temperature ($c/a = 1.603$ at 450 K), then returning to approximately the same value as at 350 K. The change in c/a ratio might point to a complex reorganization of Cu atoms during the phase transition.

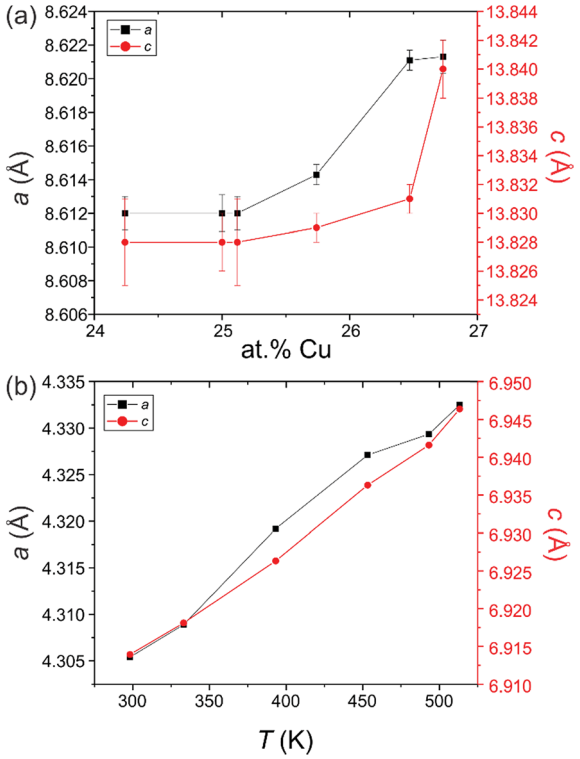

Fig. 7 (a) The room-temperature lattice parameters for YCu_xTe_2 samples with different nominal Cu content. (b) The temperature dependence of the lattice parameters for $YCu_{1.04}Te_2$, where the lattice parameters were refined for the small cell (the standard deviations are smaller than the size of the symbols used).

3.3 The electronic structure and transport properties

The computed lattice parameters of the HT-phase of $YCuTe_2$ are $a = b = 4.359$ Å and $c = 6.921$ Å. The computed band structures with and without spin–orbit coupling (SOC) effect are shown in Fig. 8a and c, respectively; we observe a determined band gap of 0.36 eV and 0.58 eV with and without the consideration of SOC effect, and in the former case a band split of ~0.7 eV occurs at the valence band maxima. This large split is due to the strong relativistic effect of Te, as the VBM is mainly comprised of Te orbitals. This type of band splitting has been observed widely in several telluride compounds such as PbTe.[49]

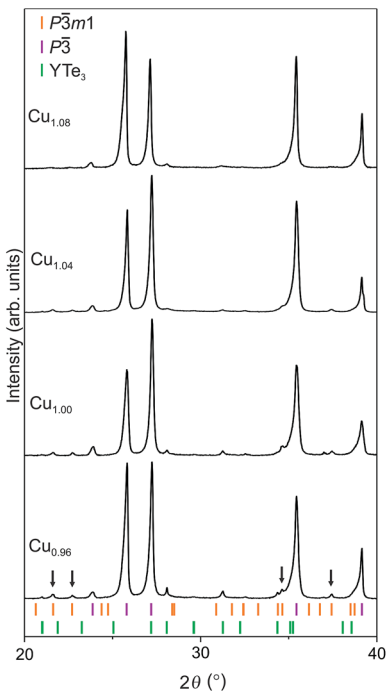

Fig. 6 XRD patterns of YCu_xTe_2 samples with different Cu content. The intensity of the main supercell reflections indicated by arrows decreases with increasing Cu content, which might lead to destruction of the partially ordered Cu arrangement and stabilize the HT-phase.

The lattice thermal conductivity was determined using the minimum thermal conductivity model of Cahill and Pohl (with computed bulk and shear moduli used to determine sound velocities), yielding κ_{min} of 0.43 W m^{-1} K^{-1}.[11,50]

Assuming a constant relaxation time of 10^{-14} s, the predicted p-type maximum average zT value over the three crystalline vectors at 600 K is 0.82 and 1.50 as determined from SOC and non-spin–orbit coupling (NSOC) electronic band structure calculations, respectively (Fig. 8b and c and Table 2). Thermal expansion has an important impact on the thermoelectric transport behaviour.[49] We also find that the maximum zT at 600 K can be enhanced through tensile strain by increasing the lattice parameter, which is accompanied with a band gap and effective mass increase (see Fig. S3† and Table 2).

The electronic transport properties were measured for the $YCuTe_2$ parent compound and the intrinsically doped samples; results are shown in Fig. 9. The electrical resistivity (ρ) increases with temperature as expected for heavily doped semiconductors (Fig. 9a). The lowest electrical resistivity was observed for the samples that contained excess Cu ($\rho \sim 4$ mΩ cm at 300 K and

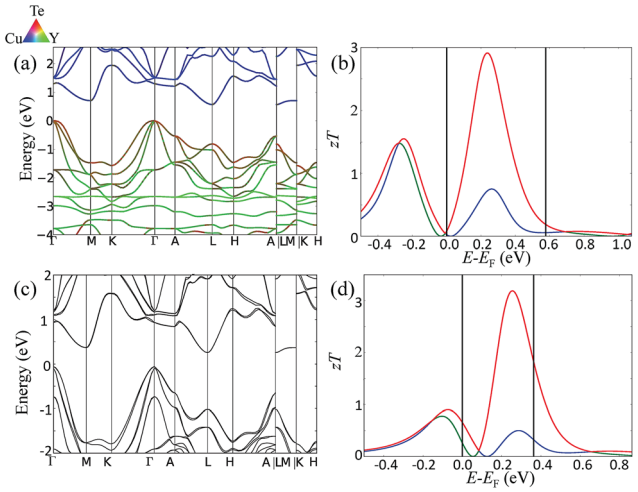

Fig. 8 (a) The electronic band structure and (b) the predicted zT at 600 K with the constant relaxation time of 10^{-14} s and a lattice thermal conductivity of 0.43 W m^{-1} K^{-1} for $YCuTe_2$ without the consideration of spin–orbit coupling; the corresponding results with the inclusion of and the SOC effect are depicted in (c) and (d). The Fermi level (E_F) corresponds to the valence band maxima.

~16 mΩ cm at 800 K), while a slightly higher electrical resistivity was observed for $YCuTe_2$ samples with lower Cu content. The electrical resistivity in all $YCuTe_2$ samples was greater than for Cu_2Te ($\rho = 0.18$ mΩ cm at 300 K)[18] and $TmCuTe_2$ ($\rho = 0.99$ mΩ cm at 300 K)[15] which is most likely due to an increased band gap energy and lower carrier concentration in $YCuTe_2$ ($E_g \sim 0.58$ eV from DFT-GGA NSOC calculation); Cu_2Te and $TmCuTe_2$ under the same theory exhibit no computed band gap ($E_g = 0$ eV) and a low band gap energy ($E_g = 0.23$ eV), respectively.[15]

The Hall mobility ($\mu_H = \frac{R_H}{\rho}$ where R_H is the Hall coefficient) is plotted as a function of temperature in Fig. 9b. μ_H for the HT phase decreases with temperature and is nearly proportional to $T^{-3/2}$, indicating that acoustic phonons are likely the dominant source of charge carrier scattering in $YCuTe_2$.[46] All samples at high temperatures had a comparable mobility whereas the mobility at room temperature depends on the composition and increases from 43 cm^2 V^{-1} s^{-1} for $YCu_{1.08}Te_2$ to 67 cm^2 V^{-1} s^{-1} for $YCuTe_2$. Two distinct regions in μ_H *versus* temperature were observed for all $YCuTe_2$ samples suggesting a phase transition from the low temperature phase to high temperature phase between 400 K and 440 K. This is in the range of the phase transition temperature as indicated in Fig. 2b.

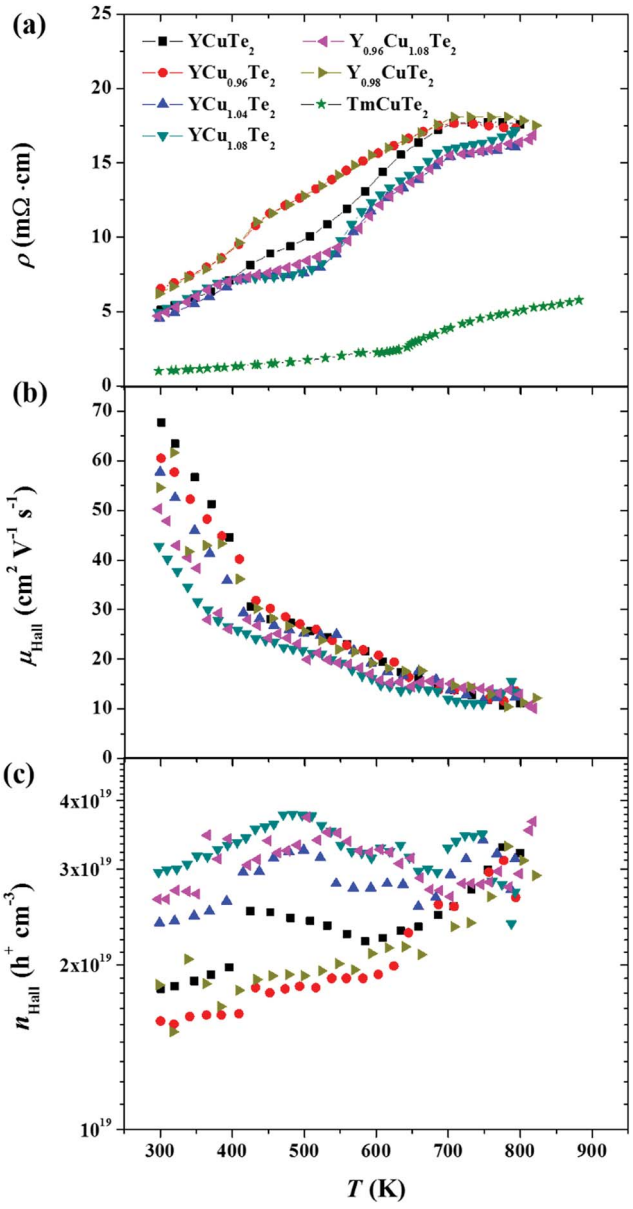

Fig. 9 Temperature dependence of (a) electrical resistivity, (b) Hall mobility, and (c) Hall carrier concentration of the $YCuTe_2$ parent compound and intrinsically doped compounds. Resistivity data for $TmCuTe_2$ is also provided for comparison.[15] The Hall carrier concentration at 300 K increases with increasing Cu content due to a decrease in the secondary phase, as shown in the SEM results in Fig. 1.

Table 2 The band gap, the hole effective mass at 600 K with carrier concentration as shown, and zT at 600 K averaged over crystalline directions with a constant relaxation time of 10^{-14} s and a lattice thermal conductivity of 0.43 W m^{-1} K^{-1} for the trigonal $YCuTe_2$ phase under different strain conditions without the consideration of SOC (the parenthetic results include SOC effects)

Strain (%)	E_g (eV)	Hole effective mass (m_0)			Max avg. p-type zT (600 K)	Carrier conc. (h$^+$ cm^{-3})
−2	0.4 (0.16)	0.31 (0.17)	0.51 (0.17)	0.51 (0.17)	1.36 (0.51)	3.04×10^{19} (3.88×10^{19})
0	0.58 (0.36)	0.36 (0.33)	0.60 (0.39)	0.60 (0.39)	1.50 (0.82)	2.22×10^{19} (3.27×10^{19})
2	0.71 (0.49)	0.45 (0.39)	0.65 (0.46)	0.65 (0.46)	1.56 (0.90)	4.0×10^{19} (2.44×10^{19})

A similar temperature dependence was observed for the Hall carrier concentration ($n_H = \frac{1}{R_H e}$ with e as elementary charge) as shown in Fig. 9c. The room temperature Hall mobility decreases with increasing Cu content (except for the parent compound) resulting in an increase in Hall carrier concentration. This behaviour is consistent with Cu_2Te, which has a lower Hall mobility ($\mu_H = 13$ cm^2 V^{-1} s^{-1} at 300 K) but a larger Hall carrier concentration ($n_H = 2.77 \times 10^{21}$ h$^+$ cm^{-3} at 300 K) than $YCuTe_2$.[18]

The positive Hall carrier concentration indicates that holes are the majority carriers in $YCuTe_2$. At room temperature, the carrier concentration increases with increasing nominal Cu content and attains the highest values for $YCu_{1.08}Te_2$. This behaviour is expected if the 'true' compositions of the compounds are considered (see Table 1). While both $YCu_{1.08}Te_2$ and $Y_{0.96}Cu_{1.08}Te_2$ are Y-deficient and slightly Cu-excess, all compounds with Cu < 1.08 have excess Y. Although the Cu content slightly increases, the presence of Y deficiency results in an overall increase in the p-type carrier concentration because Y is a trivalent cation whereas Cu is monovalent. Furthermore, the Hall carrier concentration in $YCu_{1.08}Te_2$ shows no evidence of a phase transition at 400 K as observed in the Hall mobility, and displays a maximum at around 500 K. However, the change in carrier concentration for YCu_xTe_2 with $x < 1.08$ at 400 K is most likely due to a slight shift in composition during the phase transition from a single phase to a phase-mixture region.

The temperature dependence of the Seebeck coefficient (S) is plotted in Fig. 10. The positive Seebeck coefficient confirms the Hall carrier concentration results that holes are the majority carriers. Furthermore, the Seebeck coefficient increases with temperature, with a similar temperature behaviour for all samples, to a maximum Seebeck coefficient at 780 K. While the Seebeck coefficient of the parent compound increased from 170 μV K^{-1} to 290 μV K^{-1}, $YCu_{1.08}Te_2$ has a lower Seebeck coefficient ($S = 270$ μV K^{-1} at 780 K) that can be attributed to its higher carrier concentration. For comparison, Cu_2Te and $TmCuTe_2$ both exhibit higher carrier concentrations than $YCuTe_2$, and all $YCuTe_2$ compounds have larger Seebeck coefficients than Cu_2Te (57 μV K^{-1} at 780 K)[18] and $TmCuTe_2$ (183 μV K^{-1} at 780 K).[15]

The electrical properties were compared to data calculated using the Boltzmann transport equation where the relaxation time is limited by acoustic scattering ($\tau = \tau_o(T/T_{ref})^{-3/2}(E - E_{ref})^{-1/2}$) with τ_0 fitted to the mobility data, $T_{ref} = 400$ K, and $E_{ref} = E_{VBM}$ (see Fig. S4†).

The experimental Seebeck coefficient and power factor for $YCuTe_2$ agree well with the calculated data. However, the computed Seebeck coefficient decreases at higher temperature, while the experimental Seebeck coefficient increases. The increase in Seebeck coefficient at high temperature is most likely a result of the rise in effective mass with increasing volume.

The optical properties of $YCuTe_2$ were measured using diffuse reflectance spectroscopy. Because of the large free carrier concentration in intrinsic $YCuTe_2$, the spectrum shows a broad peak at low energies. A maximum in the Kubelka-Munk function is observed at approximately 0.12 eV (Fig. 11), which corresponds to a minimum in the reflectivity associated with the plasma frequency resulting from the large free carrier concentration. The free-carrier absorption was fit to a power law and subtracted prior to considering other optical features. The effect of the free carriers decays above the maximum and is followed by another rise in the Kubelka-Munk function that we attribute to interband (valence-conduction) transitions. The extrapolated gap (assumed to be indirect as indicated by DFT calculations) is found to be ~0.6 ± 0.07 eV; however some uncertainty exists because of the unknown Burstein-Moss shift and relatively large free carrier absorption (meaning the gap could be a few k_BT smaller).[27] Temperature-dependent optical absorption edge measurements were also performed (Fig. 11 inset), which revealed a sudden decrease in the absorption edge position for $T > 450$ K (to ~0.3 ± 0.07 eV). This is consistent with the phase transition observed in the DSC (Fig. 2b) and the high-temperature XRD (Fig. 5).

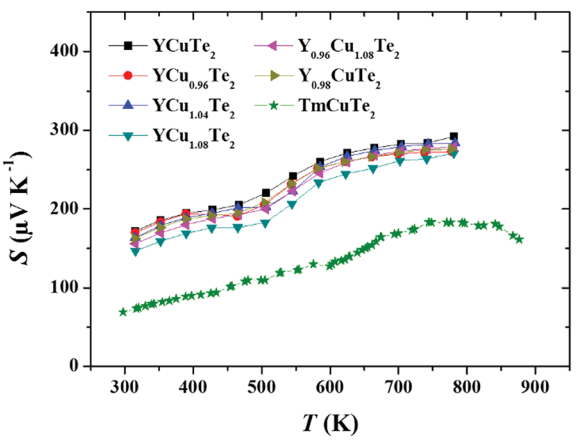

Fig. 10 The Seebeck coefficient increases with temperature for the parent $YCuTe_2$ compound and intrinsically doped samples. All investigated samples have higher Seebeck coefficient than that of $TmCuTe_2$.

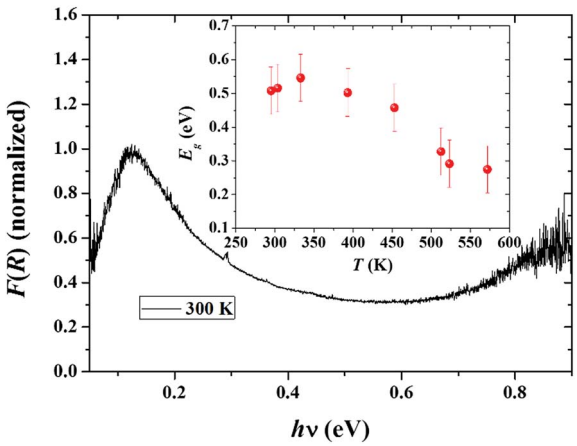

Fig. 11 Normalized optical absorption spectrum for $YCuTe_2$ at room temperature. Inset: the band gap of $YCuTe_2$ decreases above the phase transition.

3.4 Thermal transport

$YCuTe_2$, $TmCuTe_2$, and binary copper chalcogenides all undergo phase transitions. In the high-temperature phases of Cu_2S,[16] Cu_2Se,[17,18] and Cu_2Te,[18,19] the Cu ions are kinetically disordered and distributed throughout possible vacancy positions, while the anions maintain a rigid sub-lattice. The superionic Cu ions with liquid-like mobilities reduce the heat capacity as well as the thermal conductivity.[17] Conversely, in the low-temperature phases, the Cu ions are localized (non-superionic) and the crystal symmetries are lower. To check for evidence of superionic behaviour in $YCuTe_2$, the heat capacities (C_p) of the parent compound and $Y_{0.96}Cu_{1.08}Te_2$ were determined as a function of temperature (Fig. 12a). The doped sample has an almost constant heat capacity above 380 K and is slightly higher than the predicted Dulong–Petit value for $YCuTe_2$. The higher value is most likely due to the work resulting from the thermal expansion as the heat capacity at constant pressure was measured, whereas the Dulong–Petit value is C_V. The parent compound undergoes a phase transition at ~440 K in accord with the DSC (see Fig. 2b), XRD (Fig. 5) and optical results (Fig. 11). Above the phase transition, the heat capacity is constant and similar to the doped sample. No decrease in heat capacity with increasing temperature was found in the HT-phase which is dissimilar to the superionic behaviour found for $CuSe_2$.[17] Corroborating the heat capacity results, the change in enthalpy ($\Delta H = 1.7 \pm 0.2$ kJ mol^{-1}) and entropy ($\Delta S = 3.8 \pm 0.4$ J mol^{-1} K^{-1}) are small at the phase transformation and, therefore, the Cu atoms in $YCuTe_2$ should not be considered as superionic.

The thermal conductivity (κ) was determined from the measured thermal diffusivity, the mass density, and the experimental heat capacity. The temperature dependence of the thermal conductivity is plotted in Fig. 12b. The thermal conductivity decreases with increasing temperature and Cu content, which stabilizes the HT-phase (see Section 3.2). The HT-phase displays a higher Cu disorder compared to the LT-phase resulting in lower thermal conductivity as indicated by the low room temperature thermal conductivity of $YCu_{1.08}Te_2$ and $Y_{0.96}Cu_{1.08}Te_2$ ($\kappa < 1$ W m^{-1} K^{-1}). For all samples, the thermal conductivity is lower than that of $TmCuTe_2$ (ref. 15) and Cu_2Te,[18] which might be due to a higher electronic thermal conductivity contribution in those compounds.

The electronic contribution of the thermal conductivity (κ_e) was calculated by the Wiedemann–Franz law ($\kappa_e = LT/\rho$) where the Lorenz number (L) was determined from the experimental Seebeck coefficients using the single parabolic band (SPB) model.[51] The SPB model assumes that the mobility is limited by acoustic phonon scattering which was verified for $YCuTe_2$. The electronic contribution of the thermal conductivity increases with Cu content and YCu_xTe_2 samples with $x > 1$ exhibits a peak around 490 K (Fig. 12c inset).

The resulting phononic contribution of the thermal conductivity decreases with temperature. While the phononic contribution of the thermal conductivity in the YCu_xTe_2 compounds with $x \leq 1$ is proportional to $1/T$ in the temperature range from 320 K to 780 K, indicating that phonon–phonon interactions are the limiting scattering factor, YCu_xTe_2 compounds with $x > 1$ have a $1/T$ dependence above phase transition temperature of 440 K. There is no evidence of a bipolar contribution up to 780 K.

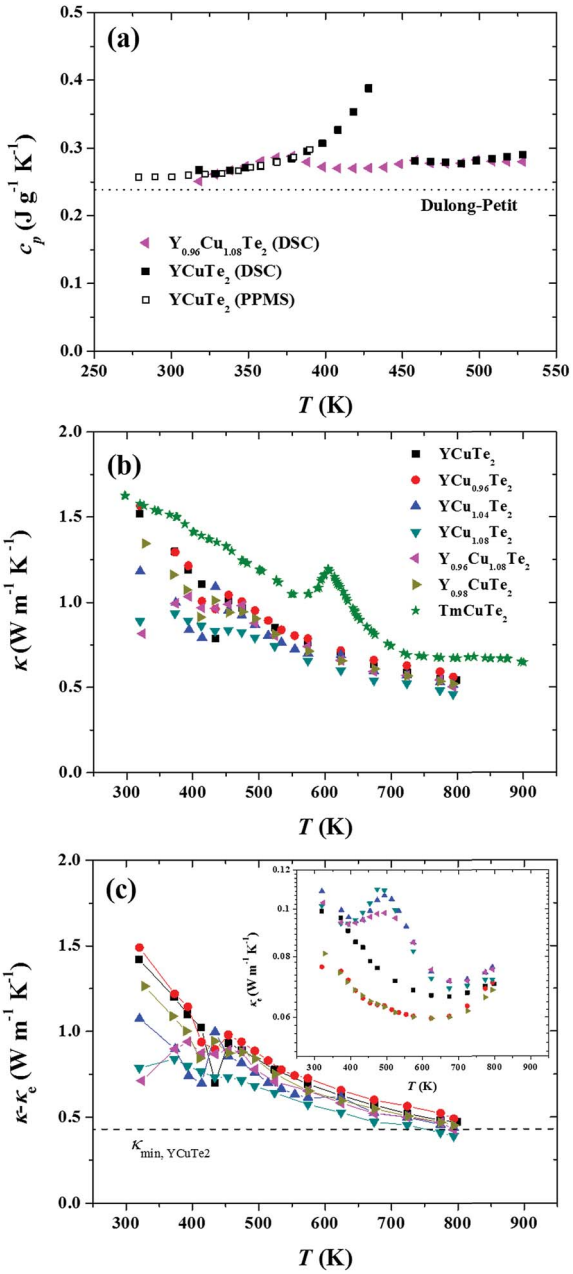

Fig. 12 (a) Heat capacity of $YCuTe_2$ (parent compound) and $Y_{0.96}Cu_{1.08}Te_2$. A phase transition was observed for the parent compound at ~440 K, whereas $Y_{0.96}Cu_{1.08}Te_2$ shows only a subtle anomaly at ~370 K, consistent with the DSC results. (b) The thermal conductivity of $YCuTe_2$ compounds decreases with increasing temperature. The room-temperature thermal conductivity decreases with increasing Cu content and decreasing Y content. All samples display lower κ than that of $TmCuTe_2$. (c) The phononic contribution of the thermal conductivity, determined from the experimental thermal conductivity with the calculated electronic contribution (see text) subtracted, approaches the predicted minimum thermal conductivity. Inset: the electronic contribution of the thermal conductivity indicates a peak for Cu-excess (YCu_xTe_2, $x > 1$) samples above the phase transition.

The lowest experimental limit of the thermal conductivity was calculated using the minimum thermal conductivity model by Cahill and Pohl and is given by:[11,50]

$$\kappa_{\min} = \frac{1}{2}\left(\frac{\pi}{6}\right)^{1/3} k_B \left(\frac{V}{N}\right)^{-2/3} (2\nu_T + \nu_L) \quad (2)$$

where k_B is Boltzmann constant, V is the unit cell volume, N is the number of atoms per unit cell, and ν_T (1870 m s^{-1}) and ν_L (3420 m s^{-1}) are the measured transverse and longitudinal speed of sounds, respectively. The calculated minimum thermal conductivity of $YCuTe_2$ (0.43 W m^{-1} K^{-1}), indicated by the dashed line in Fig. 12c, is similar to the computed minimum thermal conductivity by use of the shear and bulk moduli. For all samples, the phononic contributions of the thermal conductivity approach $\kappa_{\min}$ and $YCu_{1.08}Te_2$ is perhaps even slightly below. Therefore, the thermal conductivity is already close to the lowest limit. The lower measured thermal conductivity than the minimum thermal conductivity in $YCu_{1.08}Te_2$ might indicate overestimation of the speed of sound obtained by ultrasound measurements or an underestimation of the DFT computed sound velocities, those used to calculate the minimum thermal conductivity. In a recent study, the ultralow thermal conductivity in PCBM was described by a new minimum thermal conductivity model, where the Debye temperature was determined from the heat capacity measurements and the phonon mean free path was limited by the atomic density.[52] We computed the Grüneisen parameter (γ) of HT-$YCuTe_2$ to be 1.18, which points to high anharmonicity of the bonds similar to PbTe ($\gamma \sim 1.45$)[53] and Cu_3SbSe_4 ($\gamma = 1.22$).[54] However, this value is still lower than some other low thermal conductivity materials, *e.g.*, Cu_3SbSe_3 ($\gamma = 2.41$) and $AgSbTe_2$ ($\gamma = 2.05$) at 300 K.[55] A typical Grüneisen parameter for high anharmonicity is considered to be ~2,[56] thus, the Grüneisen parameter in $YCuTe_2$ is unlikely to be the main reason for the high C_p and low κ_L of the investigated samples.

3.5 Thermoelectric figure of merit

The thermoelectric figure of merit, zT, was calculated by polynomial fitting of the experimental electronic and thermal data. Fig. 13a indicates that zT increases with temperature for all samples. The maximum zT was observed for $Y_{0.96}Cu_{1.08}Te_2$, which reaches a value of 0.75 at 780 K. Furthermore, the maximum zT increases with increasing Cu content and decreasing Y content. A decrease in Y enhances the electronic transport properties while an increase in Cu both reduces the thermal conductivity and increases the electrical conductivity through a higher carrier concentration.

The peak figure of merit is about eight times higher than for Cu_2Te[18] and ~15% smaller than for $TmCuTe_2$.[15] We note that our zT measurements include a more accurate treatment of thermal conductivity in that we employ experimental heat capacity measurements rather than Dulong–Petit estimates; a higher zT (~0.85 at 775 K) would result from using the Dulong–Petit value.

The optimum carrier concentration can be calculated by applying the SPB model and using the Seebeck coefficient, Lorenz number, and mobility.[51] Assuming that the phononic contribution of the thermal conductivity is independent of the carrier concentration, the figure of merit is plotted as a function of the carrier concentration for the parent compound in Fig. 13b. The optimum carrier concentration is ~10^{20} cm^{-3} leading to a maximum zT of ~0.75 at 775 K. Although the carrier concentration could not be increased significantly, zT does increase somewhat with intrinsically doping due to the mobility and effective mass change.

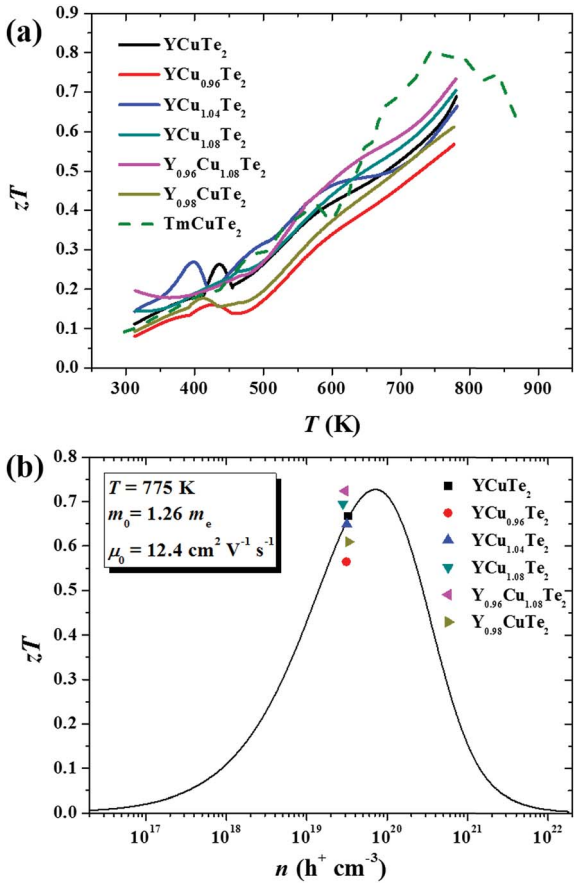

Fig. 13 (a) Thermoelectric figure of merit for $YCuTe_2$ and intrinsically doped samples. (b) The SPB model indicates that intrinsically doping with Cu can enhance the figure of merit.

4. Conclusions

Samples of intrinsically doped $YCuTe_2$ were prepared by solid state reaction of the elements. $YCuTe_2$ undergoes a first order phase transition at ~440 K from a low-temperature phase (space group $P\bar{3}m1$) to a high-temperature phase (space group $P\bar{3}$). In both crystal structures, layers of Cu–Te atoms are separated by octahedrally coordinated Y atoms. Although Cu atoms are partially ordered in the LT-phase, they are completely disordered in the HT-phase. Excess Cu content appears to favour the formation of the high temperature $P\bar{3}$ phase. All $YCuTe_2$ samples exhibit very low thermal conductivities, as low as ~0.5 W m^{-1} K^{-1} at 800 K, which is slightly above the calculated $\kappa_{\min}$. A maximum zT value of ~0.75 at 780 K was obtained for

$Y_{0.96}Cu_{1.08}Te_2$ due to favourable electronic transport resulting from Y deficiency and low thermal conductivity stemming from higher Cu disorder in the crystal structure. This observed thermoelectric efficiency is reasonably high for mid-temperature thermoelectric applications.

Acknowledgements

This work was intellectually led by the Materials Project which is supported by the Department of Energy Basic Energy Sciences program under Grant No. EDCBEE, DOE Contract DE-AC02-05CH11231. This research used resources of the National Energy Research Scientific Computing Center, a DOE Office of Science User Facility supported by the Office of Science of the U.S. Department of Energy. We would like to thank Dr Timothy Davenport for his assistance in HT-XRD measurements. U. A. acknowledges the financial assistance of The Scientific and Technological Research Council of Turkey. J.-H. P. acknowledges the Dalhousie Research in Energy, Advanced Materials and Sustainability (DREAMS) NSERC CREATE program, and M. B. Johnson's assistance. M. A. W. acknowledges the support of NSERC, and Dalhousie University's Institute for Research in Materials and its Facilities for Materials Characterization. G. H. acknowledges the F. R. S.-FNRS and the European Union Marie Curie Career Integration (CIG) grant HTforTCOs PCIG11-GA-2012-321988 for financial support. A. J. was supported by the U.S. Department of Energy, Office of Basic Energy Sciences, Early Career Research Program. Optical measurements in this work were performed at the Molecular Materials Research Center (MMRC) in the Beckman Institute at the California Institute of Technology.

Notes and references

1 Energy Flow Charts, available at:https://publicaffairs.llnl.gov/news/energy/energy.html.
2 T. M. Tritt, *Annu. Rev. Mater. Res.*, 2011, **41**, 433–448.
3 D. M. Rowe, *Thermoelectrics Handbook : Macro to Nano*, CRC; London : Taylor & Francis [distributor], Boca Raton, Fla., 2006.
4 U. Aydemir, C. Candolfi, A. Ormeci, Y. Oztan, M. Baitinger, N. Oeschler, F. Steglich and Y. Grin, *Phys. Rev. B: Condens. Matter Mater. Phys.*, 2011, **84**, 043715.
5 U. Aydemir, L. Akselrud, W. Carrillo-Cabrera, C. Candolfi, N. Oeschler, M. Baitinger, F. Steglich and Y. Grin, *J. Am. Chem. Soc.*, 2010, **132**, 10984–10985.
6 X. Shi, J. Yang, J. R. Salvador, M. F. Chi, J. Y. Cho, H. Wang, S. Q. Bai, J. H. Yang, W. Q. Zhang and L. D. Chen, *J. Am. Chem. Soc.*, 2011, **133**, 7837–7846.
7 S. M. Kauzlarich, S. R. Brown and G. J. Snyder, *Dalton Trans.*, 2007, 2099–2107, DOI: 10.1039/b702266b.
8 S. Chanakian, U. Aydemir, A. Zevalkink, Z. M. Gibbs, J. P. Fleurial, S. Bux and G. J. Snyder, *J. Mater. Chem. C*, 2015, **3**, 10518.
9 G. J. Snyder and E. S. Toberer, *Nat. Mater.*, 2008, **7**, 105–114.
10 A. Jain, S. P. Ong, G. Hautier, W. Chen, W. D. Richards, S. Dacek, S. Cholia, D. Gunter, D. Skinner, G. Ceder and K. A. Persson, *APL Mater.*, 2013, **1**, 011002.
11 D. G. Cahill and R. O. Pohl, *Annu. Rev. Phys. Chem.*, 1988, **39**, 93–121.
12 H. Zhu, G. Hautier, U. Aydemir, Z. M. Gibbs, G. Li, S. Bajaj, J.-H. Pöhls, D. Broberg, W. Chen, A. Jain, M. A. White, M. Asta, G. J. Snyder, K. Persson and G. Ceder, *J. Mater. Chem. C*, 2015, **3**, 10554.
13 L. D. Gulay, M. Daszkiewicz and V. Y. Shemet, *J. Solid State Chem.*, 2012, **186**, 142–148.
14 O. Marchuk, A. Daszkiewicz, L. D. Gulay, I. D. Ekseyuk and A. Pietraszko, *J. Alloys Compd.*, 2008, **455**, 186–190.
15 H. Lin, H. Chen, J.-N. Shen, L. Chen and L.-M. Wu, *Chem.–Eur. J.*, 2014, **20**, 15401–15408.
16 Y. He, T. Day, T. S. Zhang, H. L. Liu, X. Shi, L. D. Chen and G. J. Snyder, *Adv. Mater.*, 2014, **26**, 3974–3978.
17 H. L. Liu, X. Shi, F. F. Xu, L. L. Zhang, W. Q. Zhang, L. D. Chen, Q. Li, C. Uher, T. Day and G. J. Snyder, *Nat. Mater.*, 2012, **11**, 422–425.
18 S. Ballikaya, H. Chi, J. R. Salvador and C. Uher, *J. Mater. Chem. A*, 2013, **1**, 12478–12484.
19 N. Vouroutzis and C. Manolikas, *Phys. Status Solidi A*, 1989, **115**, 399–412.
20 D. R. Brown, T. Day, K. A. Borup, S. Christensen, B. B. Iversen and G. J. Snyder, *APL Mater.*, 2013, **1**, 052107.
21 S. Dongmin Kang, S. A. Danilkin, U. Aydemir, M. Avdeev, A. Studer and G. J. Snyder, *New J. Phys.*, 2016, **18**, 013024.
22 A. Ikeda, D. A. Kitchaev and S. M. Haile, *J. Mater. Chem. A*, 2014, **2**, 204–214.
23 L. Akselrud and Y. Grin, *J. Appl. Crystallogr.*, 2014, **47**, 803–805.
24 S. C. Mraw and D. F. Naas, *J. Chem. Thermodyn.*, 1979, **11**, 567–584.
25 D. G. Archer, *J. Phys. Chem. Ref. Data*, 1993, **22**, 1441–1453.
26 C. A. Kennedy, M. Stancescu, R. A. Marriott and M. A. White, *Cryogenics*, 2007, **47**, 107–112.
27 Z. M. Gibbs, A. LaLonde and G. J. Snyder, *New J. Phys.*, 2013, **15**, 075020.
28 K. A. Borup, E. S. Toberer, L. D. Zoltan, G. Nakatsukasa, M. Errico, J. P. Fleurial, B. B. Iversen and G. J. Snyder, *Rev. Sci. Instrum.*, 2012, **83**, 123902.
29 S. Iwanaga, E. S. Toberer, A. LaLonde and G. J. Snyder, *Rev. Sci. Instrum.*, 2011, **82**, 063905.
30 K. A. Borup, J. de Boor, H. Wang, F. Drymiotis, F. Gascoin, X. Shi, L. D. Chen, M. I. Fedorov, E. Muller, B. B. Iversena and G. J. Snyder, *Energy Environ. Sci.*, 2015, **8**, 423–435.
31 G. Kresse and J. Furthmuller, *Phys. Rev. B: Condens. Matter Mater. Phys.*, 1996, **54**, 11169–11186.
32 J. P. Perdew, K. Burke and M. Ernzerhof, *Phys. Rev. Lett.*, 1996, **77**, 3865–3868.
33 J. P. Perdew, K. Burke and M. Ernzerhof, *Phys. Rev. Lett.*, 1997, **78**, 1396.
34 P. E. Blochl, *Phys. Rev. B: Condens. Matter Mater. Phys.*, 1994, **50**, 17953–17979.
35 V. Y. Shemet, L. D. Gulay, J. Stepien-Damm, A. Pietraszko and I. D. Olekseyuk, *J. Alloys Compd.*, 2006, **420**, 58–62.

36 M. de Jong, W. Chen, T. Angsten, A. Jain, R. Notestine, A. Gamst, M. Sluiter, C. Krishna Ande, S. van der Zwaag, J. J. Plata, C. Toher, S. Curtarolo, G. Ceder, K. A. Persson and M. Asta, *Sci. Data*, 2015, **2**, 150009.
37 G. K. H. Madsen and D. J. Singh, *Comput. Phys. Commun.*, 2006, **175**, 67–71.
38 L. Vocadlo, J. P. Poirer and G. D. Price, *Am. Mineral.*, 2000, **85**, 390–395.
39 F. D. Murnaghan, *Proc. Natl. Acad. Sci. U. S. A.*, 1944, **30**, 244–247.
40 G. Hautier, A. Miglio, D. Waroquiers, G.-M. Rignanese and X. Gonze, *Chem. Mater.*, 2014, **26**, 5447–5458.
41 S. P. Ong, W. D. Richards, A. Jain, G. Hautier, M. Kocher, S. Cholia, D. Gunter, V. L. Chevrier, K. A. Persson and G. Ceder, *Comput. Mater. Sci.*, 2013, **68**, 314–319.
42 A. Jain, S. P. Ong, W. Chen, B. Medasani, X. Qu, M. Kocher, M. Brafman, G. Petretto, G.-M. Rignanese, G. Hautier, D. Gunter and K. A. Persson, *Concurrency Computat.: Pract. Exper.*, 2015, **27**, 5037–5059.
43 M. P. Pardo and J. Flahaut, *Bull. Soc. Chim. Fr.*, 1967, 3658–3664.
44 D. R. Brown, T. Day, T. Caillat and G. J. Snyder, *J. Electron. Mater.*, 2013, **42**, 2014–2019.
45 F. Gascoin, S. Ottensmann, D. Stark, S. M. Haile and G. J. Snyder, *Adv. Funct. Mater.*, 2005, **15**, 1860–1864.
46 H. Wang, Y. Pei, A. LaLonde and G. Jeffery Snyder, in *Thermoelectric Nanomaterials*, ed. K. Koumoto and T. Mori, Springer, Berlin Heidelberg, 2013, vol. 182, ch. 1, pp. 3–32.
47 L. D. Landau, E. M. Lifshits and L. P. Pitaevskiĭ, *Statistical physics*, Pergamon Press, Oxford, New York, 1980.
48 A. G. Khachaturyan, *Prog. Mater. Sci.*, 1978, **22**, 1–150.
49 H. Zhu, W. H. Sun, R. Armiento, P. Lazic and G. Ceder, *Appl. Phys. Lett.*, 2014, **104**, 082107.
50 D. G. Cahill, S. K. Watson and R. O. Pohl, *Phys. Rev. B: Condens. Matter Mater. Phys.*, 1992, **46**, 6131–6140.
51 A. F. May, E. S. Toberer, A. Saramat and G. J. Snyder, *Phys. Rev. B: Condens. Matter Mater. Phys.*, 2009, **80**, 125205.
52 J.-H. Pöhls, M. B. Johnson and M. A. White, *Phys. Chem. Chem. Phys.*, 2016, **18**, 1185–1190.
53 G. A. Slack, in *Solid State Physics*, ed. F. S. Henry Ehrenreich and T. David, Academic Press, 1979, vol. 34, pp. 1–71.
54 Y. S. Zhang, E. Skoug, J. Cain, V. Ozolins, D. Morelli and C. Wolverton, *Phys. Rev. B: Condens. Matter Mater. Phys.*, 2012, **85**, 054306.
55 D. T. Morelli, V. Jovovic and J. P. Heremans, *Phys. Rev. Lett.*, 2008, **101**, 035901.
56 B. Fultz, *Prog. Mater. Sci.*, 2010, **55**, 247–352.

